APPLIED SCIENCES AND ENGINEERING

Cascaded microfluidic circuits for pulsatile filtration of extracellular vesicles from whole blood for early cancer diagnosis

Zhenglin Li[1,2]†, Chao Liu[1,2]†, Yangchang Cheng[1,2]†, Yike Li[1,2], Jinqi Deng[1,2], Lixiao Bai[3], Lili Qin[3], Huili Mei[4], Min Zeng[4], Fei Tian[1,2]*, Shaohua Zhang[3]*, Jiashu Sun[1,2]*

Tumor-derived extracellular vesicles (EVs) hold the potential to substantially improve noninvasive early diagnosis of cancer. However, analysis of nanosized EVs in blood samples has been hampered by lack of effective, rapid, and standardized methods for isolating and detecting EVs. To address this difficulty, here we use the electric-hydraulic analogy to design cascaded microfluidic circuits for pulsatile filtration of EVs via integration of a cell-removal circuit and an EV-isolation circuit. The microfluidic device is solely driven by a pneumatic clock pulse generator, allowing for preprogrammed, clog-free, gentle, high-yield, and high-purity isolation of EVs directly from blood within 30 minutes. We demonstrate its clinical utility by detecting protein markers of isolated EVs from patient blood using a polyethylene glycol–enhanced thermophoretic aptasensor, with 91% accuracy for diagnosis of early-stage breast cancer. The cascaded microfluidic circuits can have broad applications in the field of EV research.

INTRODUCTION

Extracellular vesicles (EVs) are lipid bilayer–enclosed bioparticles with a diameter of 30 to 250 nm that are actively secreted by most mammalian cells, particularly tumor cells, into their surrounding environments and play important roles in cell-to-cell communications (*1*–*53*). Tumor-derived EVs (tEVs) carry a payload of proteins and nucleic acids reflecting the molecular characteristics of cell origin and have been abundantly found in bodily fluids such as blood. EVs are thus being recognized as a promising source of biomarkers for liquid biopsies for early cancer diagnosis and real-time monitoring of tumor development (*4*–*9*). However, a major hindrance to EV analysis is the lack of standardized, automated, and reproducible methods to isolate and purify EVs. To isolate EVs from whole blood samples, sequential centrifugation including ultracentrifugation (UC) is now the gold standard that involves multiple centrifugation steps to remove blood cells, cellular debris, and other interfering substances (*6*, *10*, *11*). The entire workflow is time-consuming and labor-intensive and requires the use of several specialized instruments. In addition, the long UC period might result in low yield of EVs with coprecipitation of protein aggregates (*12*, *13*). Several other isolation methods, such as polyethylene glycol (PEG)–based precipitation, size exclusion chromatography, immunoaffinity capture, and microfluidic separation, have been applied for isolating EVs with varied outcomes in terms of morphology, purity, and yield (*14*–*21*). Thus, there is a pressing need to develop high-performance, rapid, integrated, and cost-effective techniques for EV isolation from biological fluids.

Membrane filtration is an alternative strategy for size-selective separation of EVs by using the micro/nanoporous membranes as size exclusion filters (*22*, *23*). An exosome total isolation chip integrating several filter modules with different membrane pore sizes was reported to fractionate EVs in the size range of 30 to 200 nm from plasma and urine (*24*). A centrifugal microfluidic device containing two nanofilters allowed automated enrichment of EVs with size smaller than 600 nm from urine within 30 min (*25*). For these dead-end filtration devices, membrane fouling is a major problem that results in diminished performance with decreased recovery of EVs. In addition, the high pressure and shear force in dead-end filtration may cause damage to EVs (*26*, *27*). To reduce the filter clogging, a dual-membrane filtration method coupled with harmonic oscillations was designed for extraction of EVs from urine samples through periodic resuspension of EVs around the membrane surface (*14*). However, the application of high-frequency oscillation (3 to 7 kHz) for several tens of minutes may alter the size and integrity of EVs (*28*, *29*). Moreover, the need for complex external control system may limit the broad use of membrane filtration in clinical applications.

Here, we devise cascaded microfluidic circuits for pulsatile filtration of EVs directly from whole blood samples (Fig. 1A). The platform consists of a cell-removal circuit mounted with an external polycarbonate (PC) membrane filter (pore size of 600 nm) and an EV-isolation circuit with an anodic aluminum oxide (AAO) membrane filter (pore size of 20 nm). On the basis of the electric circuit analogy, the designed microfluidic circuits can generate pulsatile flows through the porous membrane to lift particles away from the surface, thereby inhibiting the filter fouling and particle aggregations (Fig. 1A). The microfluidic pulsatile filtration enables rapid, high-yield, and high-purity isolation of EVs in blood samples of nonmetastatic breast cancer (NMBC) within 30 min. The protein profiles of isolated EVs are measured by a one-step PEG-enhanced

[1]Beijing Engineering Research Center for BioNanotechnology, CAS Key Laboratory of Standardization and Measurement for Nanotechnology, National Center for Nanoscience and Technology, Beijing 100190, China. [2]School of Future Technology, University of Chinese Academy of Sciences, Beijing 100049, China. [3]Department of Breast Cancer, The Fifth Medical Center, Chinese PLA General Hospital, Beijing 100071, China. [4]Beijing Sihui Traditional Chinese Medicine Hospital, Beijing 100124, China.
*Corresponding author. Email: sunjs@nanoctr.cn (J.S.); zhangshaohua@csco.org.cn (S.Z.); tianf@nanoctr.cn (F.T.)
†These authors contributed equally to this work.

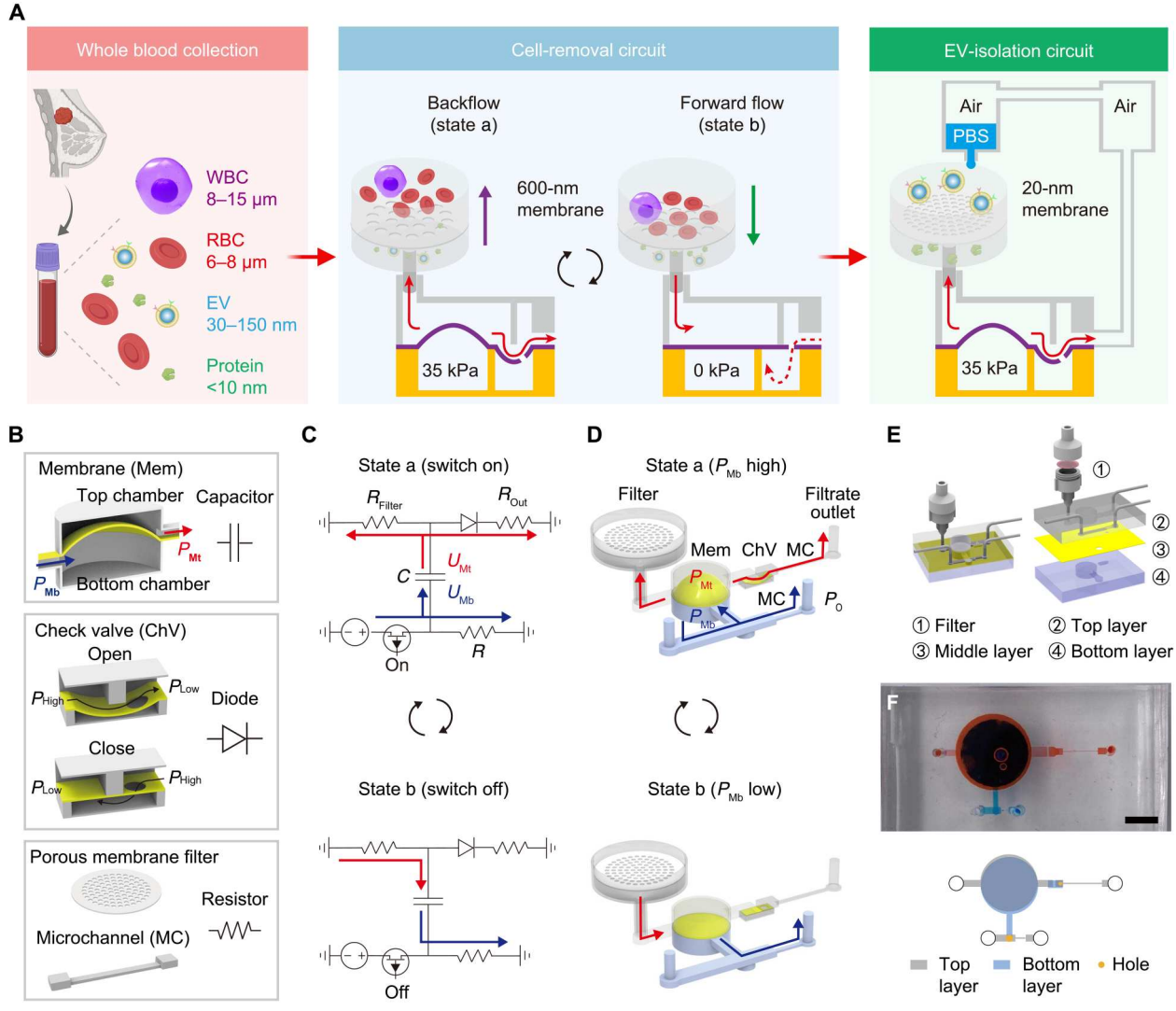

Fig. 1. Overview of pulsatile filtration of EVs. (**A**) Schematic of isolating EVs in whole blood samples by cascaded microfluidic circuits. (**B**) Microfluidic analogs to electric circuit elements. Elastomeric membrane sandwiched by microchambers is analogous to electronic capacitor, check valve to electronic diode, and microchannel/porous membrane filter to electronic resistor. (**C**) Circuit diagram and (**D**) corresponding microfluidic circuit showing the generation of pulsatile flow by switching on (state a) and off (state b) the pneumatic clock pulse generator. Red arrows indicate the flow direction of sample liquid, and blue arrows indicate the flow direction of air. P_o represents the outlet pressure that was open to the atmosphere. (**E**) Isometric view and (**F**) top view of the microfluidic device with a three-layer structure. Scale bar, 5 mm. Photo credit: Zhenglin Li, National Center for Nanoscience and Technology. U_{Mt} and U_{Mb}, voltages across capacitor; P_{Mb}, pressure of bottom microchamber; P_{Mt}, pressure of top microchamber; R_{Filter}, resistance of membrane filter; R_{Out}, resistance of microchannel connected to filtrate outlet.

thermophoretic aptasensor (pTAS) in less than 15 min for diagnosis of NMBC.

RESULTS

Working principle of microfluidic pulsatile filtration

In a manner analogous to electric circuit, the microfluidic pulsatile filtration circuit consists of fluidic capacitor, diode, and resistors integrated in a specific configuration. The fluidic capacitor is an elastomeric membrane sandwiched between the top and bottom microchambers, which can store and release the fluid upon the pressure-induced membrane deformation (Fig. 1B) (*30*, *31*). The fluidic diode is a check valve composed of a deformable membrane with a through-hole to permit fluid flow in one direction (*32*). The fluidic resistors are porous membrane (R_{Filter}) and microchannels (R_{MC}) according to the analogy between the Hagen-Poiseuille's law ($Q = P/R_{fluid}$, in which Q is flow rate, P is pressure difference, and R_{fluid} is fluidic resistance) and Ohm's law ($I = U/R_{elec}$, in which I is current, U is voltage difference, and R_{elec} is electrical resistance) (*33*, *34*). To model the microfluidic pulsatile filtration circuit, the electrical resistor–capacitor circuit with a diode is applied, in which an alternating current is passed through the capacitor and directed by the diode (Fig. 1C). The microfluidic device mimicking the electric circuit has a three-layer structure and is actuated by a pneumatic clock pulse generator (a pneumatic pump controlled by a solenoid valve). The bottom layer (also termed as the air layer) of microfluidic device is composed of an inlet connected to the pulse generator, a microchamber below the elastomeric membrane (the middle

layer), a microchannel, and a pressure outlet (the blue section in Fig. 1D). The top layer (also termed as the liquid layer) has a microchamber above the elastomeric membrane, a check valve, and a filtrate outlet. An external porous membrane filter is mounted onto the top layer (the gray section in Fig. 1D). When the pulse generator is switched on (state a), the pneumatic pressure in the bottom microchamber is suddenly increased to induce an upward deflection of the elastomeric membrane. Consequently, the liquid in the top microchamber flows to the porous membrane filter (backflow) and the filtrate outlet (red arrows in Fig. 1D, top). When the pulse generator is switched off (state b), the liquid flows from the filter to the top microchamber (forward flow) because of the recovery of the elastomeric membrane (red arrow in Fig. 1D, bottom). The pulsatile flow across the porous membrane filter is generated by periodic switching of the pulse generator. The check valve within the microfluidic device ensures that the volume of forward flow is always larger than that of backflow, leading to a time-averaged pumping flow toward the filtrate outlet. The microfluidic device with a three-layer structure is made from polydimethylsiloxane (PDMS) using the master mold fabricated by three-dimensional (3D) printing, which has a low surface roughness of <1 μm (Fig. 1, E and F, and figs. S1 and S2).

Pulsatile flow generated by the microfluidic circuit

We next used electric-hydraulic analogies to characterize pulsatile flows produced by the microfluidic circuit using the power electronics software (PLECS, Plexim GmBH, Switzerland). Dictated by the pneumatic clock pulse generator with an input pressure (P_I) of 35 kPa, an oscillating pressure ranging from 35 to 0 kPa was applied to the bottom microchamber (P_{Mb}) to deform and recover the elastomeric membrane at states a and b, respectively (Fig. 2A, top). The pressure at the top microchamber membrane (P_{Mt}) was fluctuated in response to the membrane deformation (Fig. 2A for theoretical analysis), resulting in the pulsatile flow through the porous membrane filter and the filtrate outlet at the flow rates of Q_{Filter} and Q_{Out} (red line in Fig. 2B for theoretical analysis and see the Supplementary Materials). The experimental results for Q_{Filter} and Q_{Out} were shown in fig. S3. In an oscillation cycle, the volume of forward flow ($V_{Forward}$, green area in Fig. 2B) through the filter was the sum of backflow volume at the filter (V_{Back}, purple area) and outflow volume at the filtrate outlet (V_{Out}, blue area). The ratio of V_{Out} to V_{Back} can be controlled by adjusting the hydraulic resistance of filter (R_{Filter}) and that of the microchannel connected to the filtrate outlet (R_{Out}). The simulation and experimental results showed that $V_{Forward}$ and V_{Back} through the membrane filter with pore size of 600 or 20 nm were decreased with increasing the oscillation frequency of pulse generator (Fig. 2C). V_{Out} at the filtrate outlet was also decreased with the increased frequency (Fig. 2D).

We further carried out the computational fluid dynamic (CFD) simulation to predict the flow field inside the porous membrane filter at states a and b. Using the AAO membrane with a pore size of 20 nm as an example, the time-averaged velocity of backflow at state a was 48 μm s^{-1} under the oscillation frequency of 0.5 Hz and P_I of 35 kPa (Fig. 2E). This backflow was sufficient to lift 100-nm particles away from the AAO membrane, markedly reducing the particle aggregation and membrane clogging. At state b, the forward flow with a time-averaged velocity of 95 μm s^{-1} pushed 100-nm particles toward the AAO membrane. Notably, the shear stresses around the membrane were 0.05 Pa at state a and 0.1 Pa at state b, which were lower than that in human blood vessels (>0.3 Pa) (*35*). The low shear stress during pulsatile filtration is beneficial to preserve both the morphology and function of bioparticles. These results validate the feasibility of electric-hydraulic analogy to design the microfluidic circuit for pulsatile flow filtration.

Pulsatile blood filtration by a microfluidic cell-removal circuit

After having shown the promise of pulsatile filtration, we applied the microfluidic cell-removal circuit integrated with the PC membrane filter (pore size of 600 nm) to extract plasma-containing EVs from 10-fold diluted whole blood (Fig. 3A). As shown in Fig. 3B (blue line), even with the presence of high abundancy of blood cells (hematocrit of ~4.5%), the flow rate at the filtrate outlet (Q_{Out}) remained >50% of its initial peak value (16 μl s^{-1}) after 750 s of pulsatile filtration (oscillation frequency of 0.5 Hz and P_I of 35 kPa). In sharp contrast, Q_{Out} was substantially decreased by 80% after 14 s of dead-end filtration (without pulsatile flow) and dropped to ~0 μl s^{-1} after 150 s (red line in Fig. 3B). To investigate the optimal oscillating pressure for efficient blood separation, we tested three input pressures ranging from 35 to 80 kPa with the frequency of 0.5 Hz. As shown in fig. S4, an input pressure of 55 or 80 kPa induced detectable hemolysis during the pulsatile blood filtration, whereas no hemolysis was observed at the pressure of 35 kPa. We further optimized the operating frequency in the range of 0.2 to 1 Hz under the input pressure of 35 kPa. The frequency of 0.5 Hz yielded a maximal filtration volume ($V_{Filtration}$) of ~600 μl of plasma after 1000 s (Fig. 3C and fig. S5). To estimate the membrane fouling under different filtration conditions, the modified fouling index (MFI) determined as the slope between inverse flow rate ($t/V_{Filtration}$) and $V_{Filtration}$ was assessed (*36*–*38*). The MFI value of the dead-end filtration in which blood cells continuously blocked the pores was higher than that of pulsatile filtration attributed to the periodical backflows to prevent pore blocking (Fig. 3D). In the pulsatile filtration, the oscillation frequency of 0.5 Hz showed the highest $V_{Filtration}$ and the lowest membrane fouling, indicating an improved antifouling performance. We also analyzed the level of hemolysis of filtered plasma samples by measuring the absorption spectra of hemoglobin. As depicted in Fig. 3 (E and F), apparent hemolysis could be detected in filtered samples from dead-end filtration, whereas no detectable hemolysis was found in plasma samples from pulsatile filtration at the investigated frequencies (0.2 to 1 Hz). Bright-field microscope images in Fig. 3G revealed that blood cells including leukocytes and erythrocytes could be effectively eliminated at the optimal condition (35 kPa, 0.5 Hz). The cell enumeration by an automatic cell counter (Countess 3, Invitrogen) suggested a >4 orders of magnitude depletion of blood cells, equivalent to 99.99% removal of cells (Fig. 3H). Thus, pulsatile filtration with the microfluidic cell-removal circuit is a powerful tool to fractionate plasma from whole blood.

Pulsatile filtration of EVs by a microfluidic EV-isolation circuit

For EV isolation and purification, an AAO membrane filter (pore size of 20 nm) was integrated with a microfluidic EV-isolation circuit, which has the same microfluidic architecture as the cell-removal circuit (Fig. 4A). In addition, a circulating washing system was combined with the EV-isolation circuit to purify EVs and prevent the loss of EVs from the drying of membrane filter (*39*). The washing system consisted of two serially connected

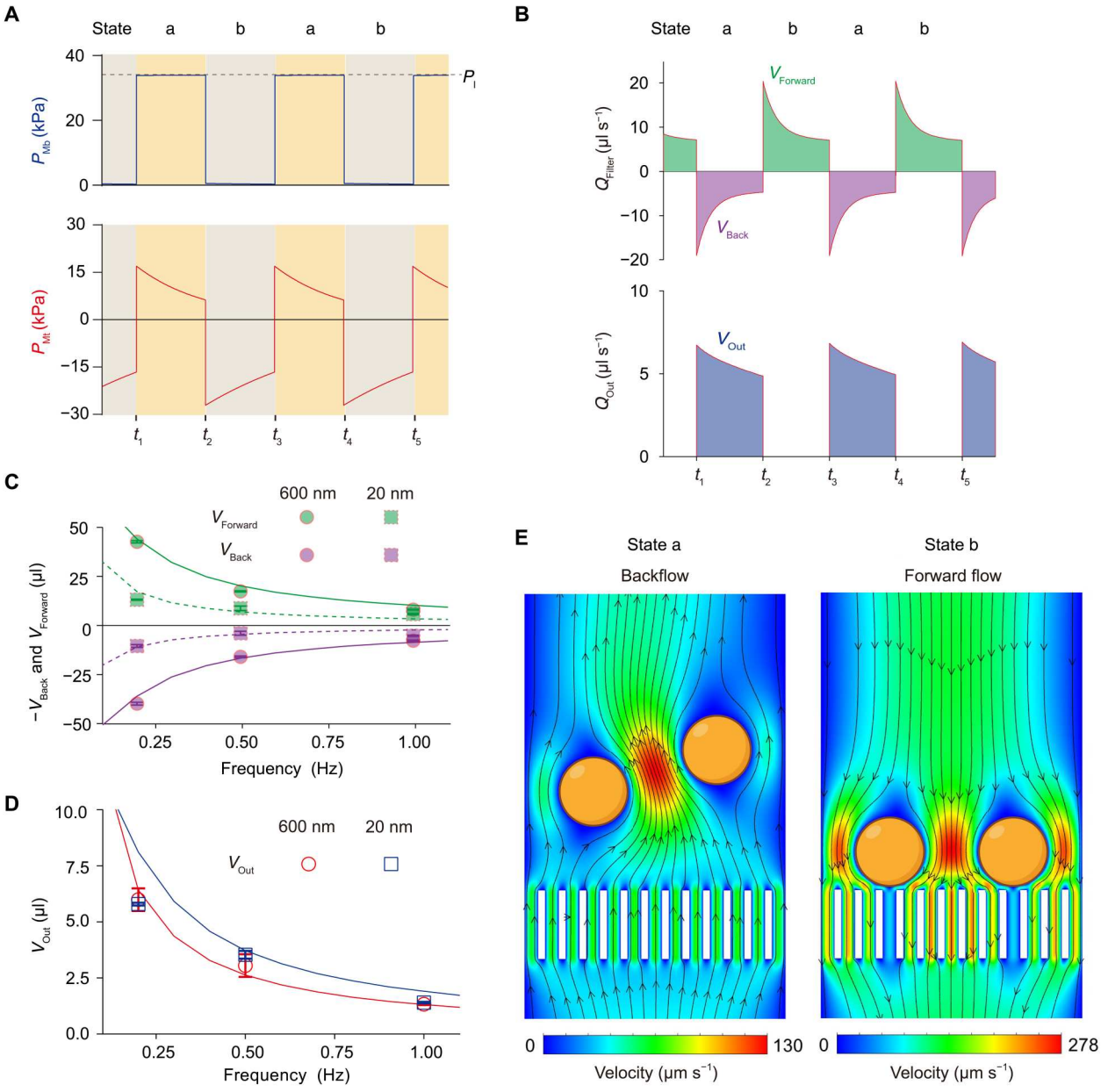

Fig. 2. Characterization of pulsatile flow generated by the microfluidic circuit. (**A**) Pressure profiles of the bottom microchamber (P_{Mb}) and the top microchamber (P_{Mt}) separated by the elastomeric membrane. (**B**) Flow rates at the porous membrane filter (Q_{Filter}) and the filtrate outlet (Q_{Out}). The volumes of forward flow ($V_{Forward}$), backflow (V_{Back}), and outflow (V_{Out}) in an oscillation cycle are indicated by green, purple, and blue areas, respectively. (**C**) Experimental (points) and simulation results (lines) of V_{Back} (purple) and $V_{Forward}$ (green) through the membrane filter with pore size of 600 nm (circles) or 20 nm (squares) (n = 3 independent technical replicates, means ± SD). (**D**) Experimental (points) and simulation results (lines) of V_{Out} at the filtrate outlet (n = 3 independent technical replicates, means ± SD). Red and blue colors indicate the use of 600 and 20 nm porous membrane filters, respectively. (**E**) CFD simulation of the flow field across the AAO membrane with pore size of 20 nm. At state a, the backflow lifts 100-nm particles away from the membrane. At state b, the forward flow pushes 100-nm particles toward the membrane. Yellow circles indicate the 100-nm particles. Lines and arrows indicate streamlines and flow directions, respectively.

containers: One container was prefilled with phosphate-buffered saline (PBS), and the other empty one was for waste filtrate and connected to the outlet of microfluidic circuit. In the process of pulsatile filtration, the waste filtrate was pneumatically pumped into the empty container, actuating an equal volume of prefilled PBS to drip onto the membrane filter. The two containers were separated by air to prevent cross contamination, and the circulating washing system was sealed with tubes and needles.

The microfluidic pulsatile filtration was characterized by isolating EVs from cell culture medium (CCM) of MCF-7 (breast cancer cell line), SK-BR-3 (breast cancer cell line), or MCF-10A (mammary epithelial cell line). The concentrations of MCF-7 EVs, SK-BR-3 EVs, and MCF-10A EVs in CCM ranged from 5.0×10^9 to

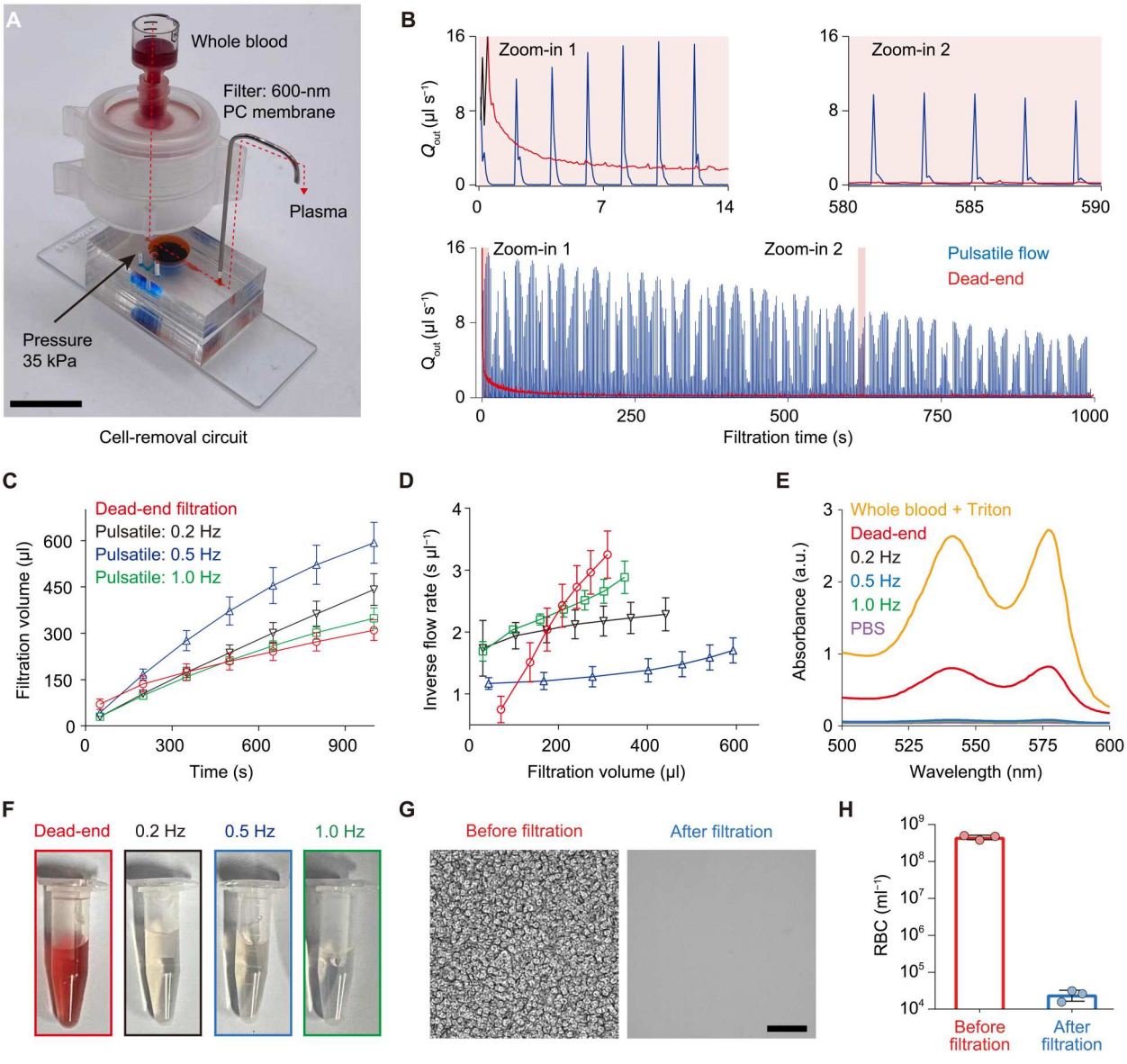

Fig. 3. Pulsatile blood filtration by a microfluidic cell-removal circuit. (**A**) Photograph of the microfluidic circuit integrated with the PC membrane filter (pore size of 600 nm) for plasma extraction from diluted whole blood. Scale bar, 20 mm. (**B**) Flow rate at the filtrate outlet (Q_{Out}) of the pulsatile filtration (blue line) and dead-end filtration (without pulsatile flow, red line). (**C**) Filtration volume ($V_{Filtration}$) of plasma as a function of time in the pulsatile filtration at various frequencies and dead-end filtration (n = 3 independent technical replicates, means ± SD). (**D**) MFI to estimate the membrane fouling under different filtration conditions (n = 3 independent technical replicates, means ± SD). (**E**) Absorbance spectra of hemoglobin in filtered samples under pulsatile and dead-end filtration. Whole blood spiked with 0.1% Triton X-100 for blood cell lysis was used as the positive control. (**F**) Photographs of the filtered samples under the pulsatile and dead-end filtration. (**G**) Bright-field microscope images of diluted whole sample before and after the pulsatile filtration at 0.5 Hz and P_I of 35 kPa. Scale bar, 50 μm. (**H**) Cell counting analysis indicating 99.99% depletion of blood cells after the pulsatile filtration (n = 3 biological replicates, means ± SD). The sample diluted by 1000-fold before filtration and the samples after filtration without dilution were used for cell counting by an automatic cell counter. Photo credit: Zhenglin Li, National Center for Nanoscience and Technology. RBC, red blood cell; a.u., arbitrary units.

7.8×10^9 ml^{-1}, measured by nanoparticle tracking analysis (NTA; Fig. 4B). After concentrating 3 ml of CCM into 200 μl via the pulsatile filtration with circulating washing, the concentrations of EVs were increased to 5.7×10^{10} to 1.2×10^{11} ml^{-1} (35 kPa, 0.5 Hz), whereas the concentrations of EVs by the dead-end filtration (35 kPa, without pulsatile flow) were in the range from 1.2×10^{10} to 5.0×10^{10} ml^{-1}. The recovery rate of EVs was from 76.3 to 91.7% with a low coefficient of variation (CV; 9.4%) by pulsatile filtration, as compared with that of 18.5 to 42.8% for dead-end filtration with a CV of 39.3% (Fig. 4C). Notably, the cell line EVs isolated by UC showed a recovery rate of 25.1 to 34.4% (CV of 16.6%). Figure 4D and fig. S6 indicated that the mean sizes of MCF-7 EVs, SK-BR-3 EVs, and MCF-10A EVs after the pulsatile filtration and dead-end filtration were similar to those in CCM (119 nm for MCF-7 EVs, 94 nm for SK-BR-3 EVs, and 118 nm for MCF-10A EVs). However, the mean size of cell line EVs was increased by 1.2- to 1.7-fold after UC,

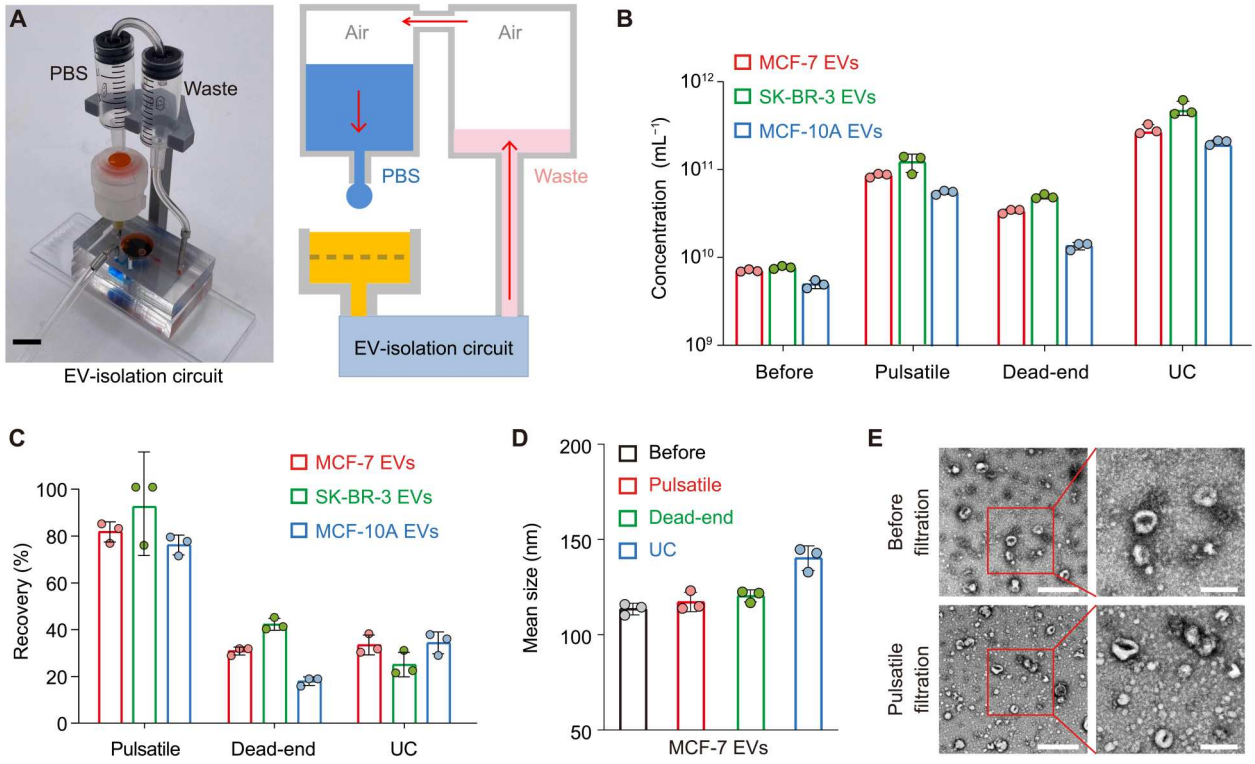

Fig. 4. Pulsatile filtration of EVs by a microfluidic EV-isolation circuit. (**A**) Photograph and schematic of the microfluidic circuit integrated with an AAO membrane filter (pore size of 20 nm) and a circulating washing system for EV isolation from CCM. Scale bar, 10 mm. (**B** and **C**) Comparison of concentration (B) and recovery rate (C) of EVs isolated from CCM by different EV isolation methods ($n = 3$ independent technical replicates, means ± SD). The CCM of two breast cell lines (MCF-7 and SK-BR-3) and a mammary epithelial cell line (MCF-10A) were used. UC indicates ultracentrifugation. (**D**) Comparison of mean size of MCF-7 EVs isolated from CCM by different isolation methods ($n = 3$ independent technical replicates, means ± SD). (**E**) TEM images of MCF-7 EVs before and after the pulsatile filtration with circulating washing (1 ml of PBS). Scale bars, 500 nm (zoom-in, 200 nm). Photo credit: Zhenglin Li, National Center for Nanoscience and Technology.

possibly due to the high gravity of UC that may cause EV loss, aggregates, and fusions (*40*). To assess the integrity of EVs, we recorded the fluorescence images of 3,3-dioctadecyloxacarbocyanine perchlorate–labeled MCF-7 EVs before and after the pulsatile filtration. As expected, a large number of fluorescent dots corresponding to MCF-7 EVs were seen after filtration, while no fluorescent dots were observed for dimethyl sulfoxide–treated EVs due to the complete membrane disruption (fig. S7). Moreover, the transmission electron microscope (TEM) images of isolated MCF-7 EVs by pulsatile filtration showed the characteristic cup-like shape, indicating that the gentle microscale flow filtration could prevent damage to EVs (Fig. 4E). We further performed Western blot (WB) to characterize the expression of three protein markers—cluster of differentiation 81 (CD81; a transmembrane protein and an EV marker), tumor susceptibility gene 101 (TSG101; a cytosolic protein and an EV marker), and calnexin (protein not enriched in EVs) on CCM EVs. WB analysis of the enriched EVs by pulsatile filtration demonstrated the presence of both CD81 (the 25-kDa band) and TSG101 (the 44-kDa band) and the absence of calnexin (the 100-kDa band; fig. S8). In comparison, no expression of CD81, TSG101, and calnexin was observed before pulsatile filtration due to the low abundance of EVs in CCM.

Isolation of EVs from blood samples by cascaded microfluidic circuits

We next integrated the microfluidic cell-removal circuit and the EV-isolation circuit for pulsatile filtration of EVs directly from blood samples (Fig. 5). To cascade the two microfluidic circuits, the filtrate outlet of cell-removal circuit was connected to the inlet of AAO membrane filter of EV-isolation circuit via a connecting tube (Fig. 5A). In this manner, the filtered plasma from blood by the cell-removal circuit was subsequently processed by the EV-isolation circuit. For pulsatile filtration of EVs from plasma, the optimal frequency was determined to be 0.5 Hz, as indicated by the highest washing volume of PBS (Fig. 5B). To estimate the removal efficiency (ξ) of soluble proteins by pulsatile filtration with circulating washing, a theoretical model was developed as follows

$$\xi = \left[1 - \left(\frac{V_{\text{Loading}} - V_{\text{Droplet}}}{V_{\text{Loading}}}\right)^{N}\right] \times 100\% \quad (1)$$

where V_{Loading} is the volume of sample, V_{Droplet} is the volume of a single PBS droplet, and N is the number of droplets dripping onto the membrane filter. For V_{Droplet} of 27 μl measured by a high-precision pipette, the decrease of V_{Loading} and the increase of N yielded an increase of the ξ. To validate the theoretical analysis, we loaded 200 μl of bovine serum albumin (BSA) solution (1.4 mg ml^{-1}) into

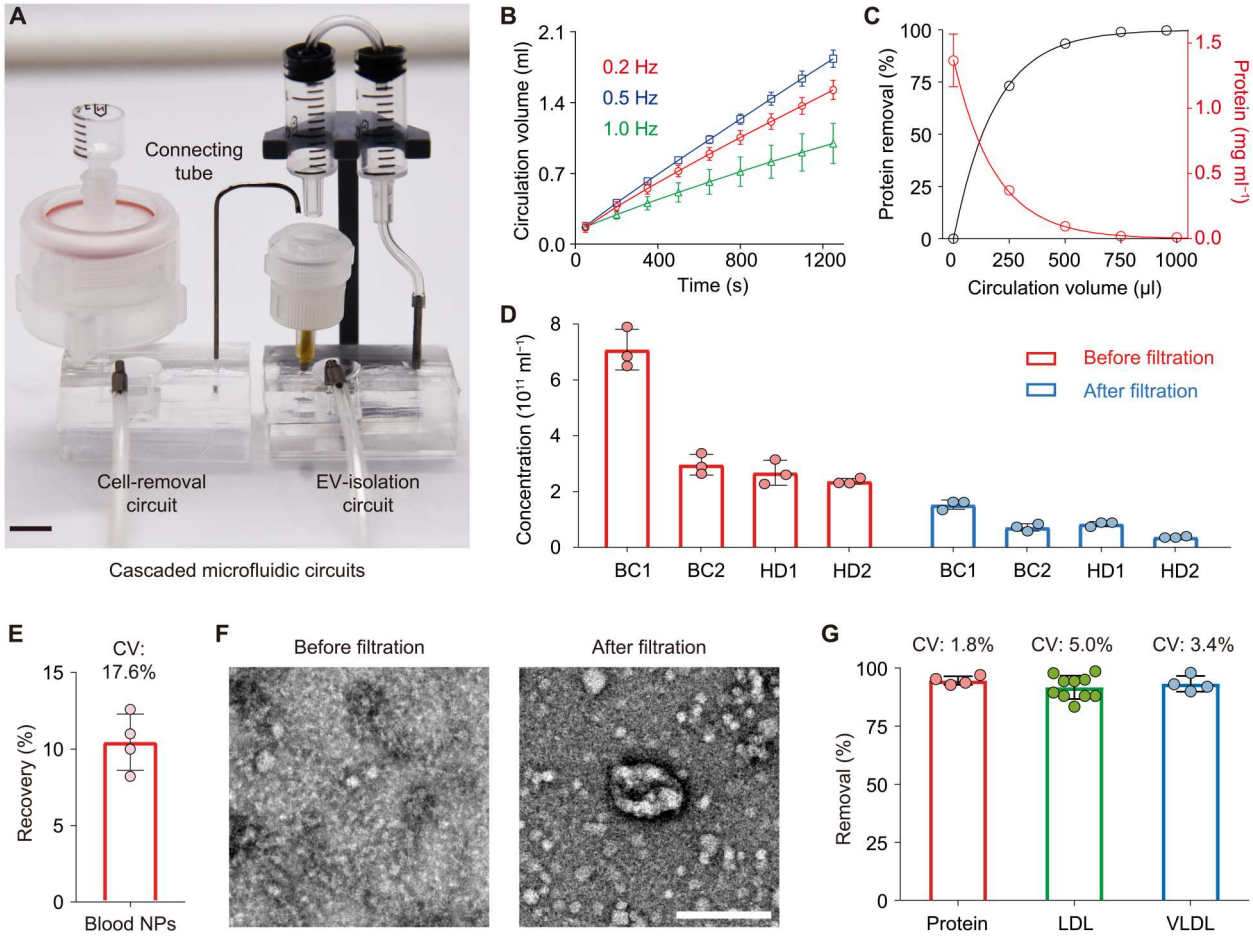

Fig. 5. Isolation of EVs from whole blood samples by cascaded microfluidic circuits. (**A**) Photograph of the cascaded microfluidic circuits consisting of the cell-removal circuit and the EV-isolation circuit for isolating EVs directly from whole blood. Scale bar, 10 mm. (**B**) Washing volume of PBS as a function of time in the pulsatile filtration at different frequencies ($n = 3$ independent technical replicates, means ± SD). Two hundred microliters of 50-fold–diluted blood plasma was initially loaded on the AAO membrane filter (pore size of 20 nm). (**C**) Removal efficiency of soluble protein as a function of PBS volume for circulating washing using AAO membrane filters ($n = 3$ independent technical replicates, means ± SD). Points and lines indicate experimental measurements and theoretical predictions, respectively. Black and red colors indicate protein removal efficiency and protein concentration, respectively. (**D**) Concentrations of NPs before and after the cascaded pulsatile filtration of blood samples from two patients with NMBC and two HDs ($n = 3$ independent technical replicates, means ± SD). (**E**) Recovery rate of NPs by pulsatile filtration ($n = 4$ biological replicates, means ± SD). (**F**) TEM images of isolated EVs from blood. Scale bar, 200 nm. (**G**) Removal efficiencies of protein (red, $n = 4$ biological replicates, means ± SD), LDL (green, $n = 10$ biological replicates, means ± SD), and VLDL (blue, $n = 4$ biological replicates, means ± SD) from blood samples by cascaded microfluidic circuits. Photo credit: Zhenglin Li, National Center for Nanoscience and Technology.

the AAO membrane filter and used different volumes of PBS (250, 500, 750, and 1000 μl) to estimate the ξ of BSA by pulsatile filtration (35 kPa, 0.5 Hz). As seen in Fig. 5C, increasing the washing volume of PBS was associated with the increase of ξ of BSA, and the ξ of >99% was achieved with 1000 μl of PBS ($N = 37$). Moreover, the experimental result was consistent with the theoretical analysis of the ξ.

To characterize the performance of cascaded microfluidic circuits, four whole blood samples (10-fold dilution, 200 μl each) from two patients with NMBC and two healthy donors (HDs) were tested at the optimal condition (35 kPa and 0.5 Hz for both circuits, 1000 μl of PBS for circulation washing), and the purified EVs were concentrated to 100 μl via an additional step of pulsatile filtration. The entire process of isolation and purification of EVs from whole blood was completed within 30 min. Figure 5D showed that the concentrations of bio-nanoparticles (NPs) after cascaded pulsatile filtration ranged from 3.7×10^{10} to 1.5×10^{11} ml^{-1}. The recovery rate of NPs was determined to be approximately 10.5% with a CV of 17.6% (Fig. 5E). TEM images suggested that EVs could be successfully isolated from whole blood samples by cascaded microfluidic circuits (Fig. 5F and fig. S9). Meanwhile, the microfluidic pulsatile filtration revealed a removal efficiency of ~95% for protein contents (Fig. 5G). We further investigated the ability of cascaded microfluidic circuits to deplete low- and very low–density lipoproteins (LDLs and VLDLs) from blood. LDL and VLDL are major confounding factors in EV research due to their overlap in size. As summarized in Fig. 5G, the removal efficiency of VLDL from 4 blood samples was 90 to 98% (CV of 3.4%) and that of LDL was 83 to 99% (CV of 5.0%) for 10 blood samples after microfluidic pulsatile filtration. Note that the low recovery of NPs from blood may be associated with the effective removal of LDL and VLDL, indicating a high purity of the isolated EVs. Together,

the cascaded microfluidic circuits demonstrate a marked enhancement in isolating EVs directly from whole blood samples with high removal efficiencies of soluble proteins, LDL, and VLDL.

Protein detection of isolated EVs by pTAS

To measure the surface proteins of EVs isolated by cascaded microfluidic circuits, we developed a one-step pTAS (*41*, *42*). As depicted in Fig. 6A, EVs were first mixed with Cy5-conjugated aptamer targeting epithelial cellular adhesion molecule (EpCAM; a tumor marker) or CD63 (a pan-EV marker) and PEG molecules (8 kDa, 7.5%), and the mixture was transferred to a customized microchamber. An infrared laser (1480 nm) was focused on the center of microchamber to create a temperature gradient and a PEG concentration gradient, allowing for simultaneous aptamer binding to EV proteins and size-selective accumulation of EVs at the laser spot within 10 min (Fig. 6A). The pTAS was first used to detect the protein expression in different types of cell line EVs. MCF-7 EVs and SK-BR-3 EVs that were derived from EpCAM-positive cell lines with epithelial phenotypes exhibited an ~10-fold increase in the expression of EpCAM as compared to that of MCF-10A EVs from EpCAM-negative cell line (Fig. 6, B and C). In addition, the levels of CD63, a widely used marker for EVs, were similar in three types of EVs measured by pTAS (Fig. 6, B and C). The performance of pTAS for detecting EV EpCAM and CD63 was also verified by WB, and a good concordance between two methods was observed (fig. S10). The fluorescence intensity of EpCAM on SK-BR-3 EVs measured by pTAS was linear over an EV concentration range of 5×10^9 to 10^{11} ml^{-1} (Fig. 6D). The estimated limit of

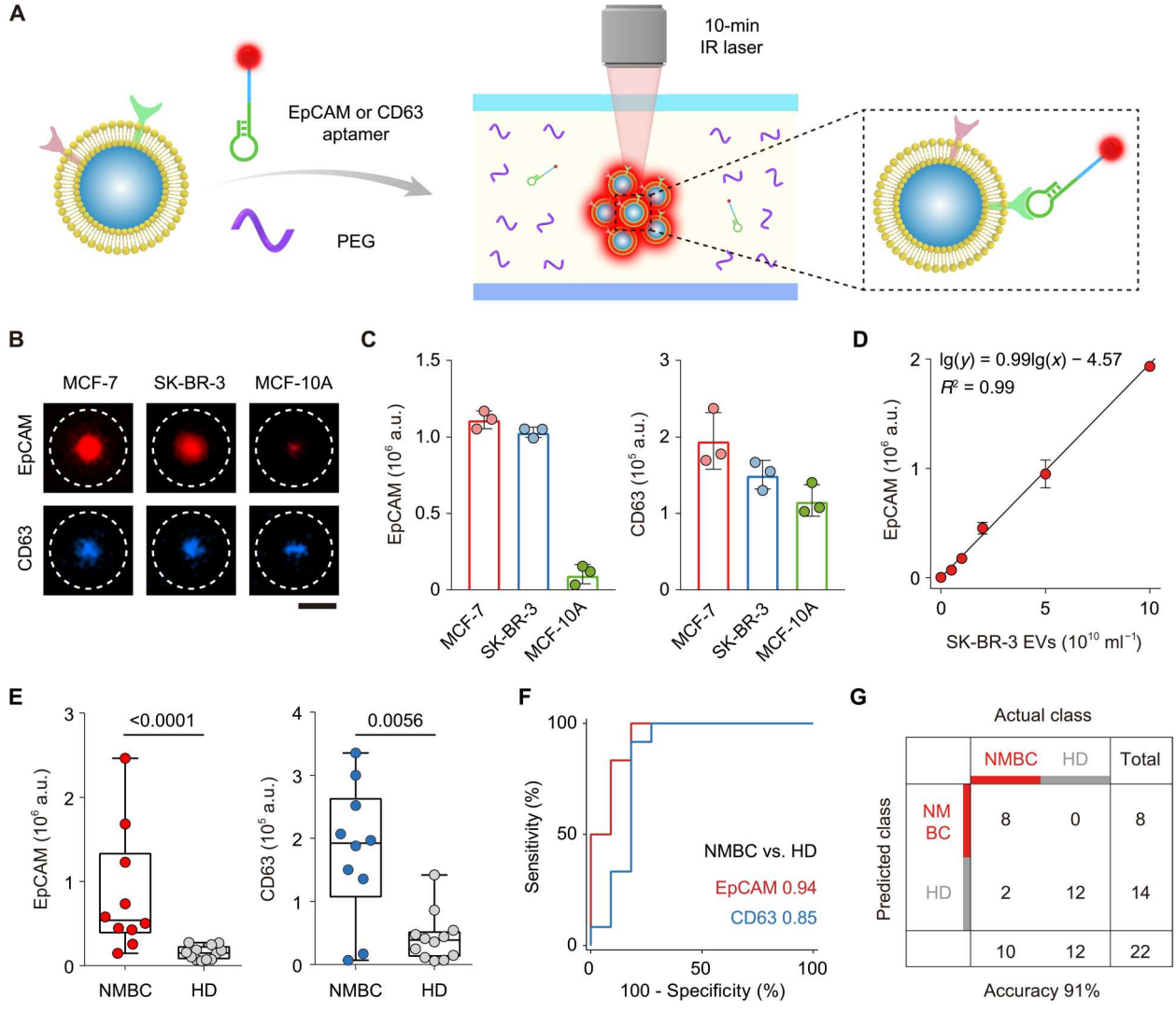

Fig. 6. Detection of EV proteins by pTAS. (**A**) Schematic illustration of the pTAS for one-step detection of surface proteins of EVs. IR, infrared. (**B**) Fluorescence images of pTAS for detecting MCF-7 EVs, SK-BR-3 EVs, and MCF-10A EVs using EpCAM or CD63 aptamers. Scale bar, 10 μm. (**C**) Expression levels of EpCAM and CD63 on cell line EVs measured by pTAS ($n = 3$ independent technical replicates, means ± SD). (**D**) Sensitivity and linear range of pTAS for detecting EpCAM on SK-BR-3 EVs ($n = 3$ independent technical replicates, means ± SD). R^2, coefficient of determination. (**E**) Scatter plots showing the EpCAM and CD63 expression levels of EVs isolated from whole blood samples by cascaded microfluidic circuits ($n = 10$ biological replicates for NMBC patients and $n = 12$ biological replicates for HD). (**F**) ROC analysis of EV EpCAM and EV CD63 between NMBC and HD cohorts. (**G**) Confusion matrix showing the accuracy of EV EpCAM for NMBC versus HD discrimination. The *P* value in (E) was determined by two-tailed Mann-Whitney *U* test.

detection of 1.3×10^8 ml^{-1} was sufficient to detect blood EVs ranging from 10^{10} to 10^{12} ml^{-1} (*43*, *44*).

Being able to detect EV proteins, we extended the cascaded microfluidic circuits and pTAS for isolating and detecting EVs directly from blood samples ($n = 10$ for NMBC patients and $n = 12$ for HD). The expression levels of EpCAM and CD63 on EVs in the NMBC cohort were statistically higher than those in the HD cohort ($P < 0.0001$ for EpCAM and $P = 0.0056$ for CD63) (Fig. 6E). Using receiver operating characteristic (ROC) analysis between NMBC and HD cohorts, we found that EV EpCAM had a higher value of area under the ROC curve (AUC; 0.94) than that of CD63 (AUC of 0.85; Fig. 6F). The confusion matrix in Fig. 6G showed that EV EpCAM had an accuracy of 91% (20 of 22) for NMBC versus HD discrimination.

DISCUSSION

Among a wide variety of biomarkers in blood samples, tEVs carry a rich set of molecular contents from parental cells, emerging as a more reflective biomarker for cancer diagnosis and prognosis (*45*–*47*). However, the small size of EVs and high quantities of blood cells, soluble proteins, and lipoproteins in whole blood pose a challenge in the isolation and analysis of EVs (*48*, *49*). Current approaches such as UC and advanced sorting methods rely on extensive and laborious procedures and face the issues of low recovery rate of EVs and contamination with protein aggregates. For biochemical analysis of EVs, conventional enzyme-linked immunosorbent assay (ELISA) or WB are performed using a multistep protocol, impeding the translation of EVs in clinical setting (*50*). To fully explore the utility of EVs, there is a clear need to isolate and analyze EVs from blood samples in a rapid and integrated manner.

In this work, we used the hydraulic-electric analogy to devise cascaded microfluidic circuits integrated with a PC membrane filter (pore size of 600 nm) and an AAO membrane filter (pore size of 20 nm) for isolation and purification of EVs directly from blood samples. The microfluidic device required only 60 μl of raw blood sample, which was diluted by 10-fold before filtration. The minimal volume that the device can work with was 100 μl. The periodic pulsatile flow generated by the device repeatedly levitated bioparticles away the membrane filter to reduce membrane fouling while keeping higher EV yield and purity than gold standard UC and conventional dead-end filtration. In addition to the field of EV isolation, the presented approach is readily implemented in membrane filtration of circulating tumor cells in whole blood samples by using the cell-removal circuit with a membrane filter (pore size of 8 to 12 μm). Compared with other microfluidic filtration devices that often require numerous control systems (e.g., flow control system, electronics, etc.) (*14*), our microfluidic pulsatile filtration is solely driven by a pneumatic clock pulse generator, eliminating the need for complex external equipment. Moreover, the pulsatile filtration can process whole blood directly with high throughput, whereas most separation techniques rely on complex preprocessing steps. In addition, our microfluidic device and filter holder are reusable after suitable washing (fig. S11), and the architecture of microfluidic devices is highly modular as the microfluidic circuits can be flexibly cascaded. Overall, the pulsatile microfluidic membrane filtration displays efficient and robust isolation and will have a distinct improvement in the field of microfluidic membrane filtration.

Furthermore, we developed pTAS for rapid, sensitive, and one-step measurement of the surface proteins of isolated EVs (table S1). As the recognition probes, merits of aptamers include small steric hindrance and high thermal stability that favor the binding of proteins on nanoscale EVs for thermophoretic detection (*51*, *52*). Using an infrared laser irradiation to induce sharp gradients of temperature and PEG concentration, pTAS leveraged the high level of accumulation of EVs (over 10^3-fold) by PEG-enhanced thermophoresis and fast kinetics of the binding of fluorescent aptamers to EV proteins, resulting in an amplified fluorescence signal proportional to the expression of target proteins on EVs within 10 min. Besides, pTAS was carried out under homogenous reaction conditions benefiting from the size-dependent accumulation of EVs by thermophoresis, avoiding multiple washing steps to remove the unbound aptamers of small sizes (a few nanometers).

Despite these promising results, the cascaded pulsatile filtration can be further improved from several aspects in future studies. First, the system currently processes one blood sample per run. By exploiting the good scalability of microfluidic circuit, efforts can be drawn to develop compact chips integrating multiple filtration units. Second, the EV isolation and downstream biomarker analysis can be streamlined in a single microfluidic device by using the electric circuit analogy to design a sequential-flow system (*31*, *53*–*55*), which may further simplify the personnel operation, improve the reproducibility, and reduce the assay time. Last, although the microfluidic pulsatile filtration removed ~95% of protein contents, ~92% of LDL, and ~93% of VLDL from blood samples, there may be still a considerable amount of proteins and other bioparticles contaminating the isolated EVs.

In summary, we presented cascaded microfluidic circuits for rapid isolation of EVs directly from whole blood samples with high yield and purity (table S2). The protein profiles of isolated EVs were detected by pTAS for accurate noninvasive diagnosis of early-stage breast cancer. The entire workflow was completed within 45 min, showing great potential to improve the cancer diagnosis by EV-based liquid biopsy.

MATERIALS AND METHODS

Microfluidic device design and fabrication

The microfluidic device consists of three PDMS layers: a top layer, a bottom layer, and a 50-μm-thick elastomeric membrane as the middle layer. The top layer is composed of a microchamber above the elastomeric membrane, a check valve, a filtrate outlet, and a microchannel connected to the filtrate outlet. The bottom layer is composed of a microchamber below the elastomeric membrane, an inlet connected with the pulse generator, a pressure outlet, and T-shaped microchannels interconnecting the bottom microchamber, the inlet, and the pressure outlet. The middle layer has a through-hole allowing for flow along only one direction. The detailed dimensions of key microfluidic components are summarized in table S3. The top and bottom layers were replicated from a master mold that was fabricated using a 3D printer (UV Max, Asiga, Australia). Before 3D printing, a glass slide as the mold substrate was treated by 3-(trimethoxysilyl)propyl methacrylate (T1601, Innochem, China) for 30 min. The glass slide was then fixed on the 3D printer with double-sided tapes. Resins (PlasGray, Asiga, Australia)

were directly printed onto the glass slide to prevent the resin deformation during heating. After 3D printing, the resultant mold was irradiated with ultraviolet (UV) light using a UV curing system (DR-301C, Asiga, Austrilia) for 30 min and then baked in an oven at 80°C overnight. The degassed mixture of PDMS and curing agent (Sylgard, USA) at a ratio of 10:1 was cast over the master mold and baked in an oven at 80°C for 2 hours. The obtained top and bottom layers were punched with biopsy punches (1.5 and 1 mm; Miltex, Germany) for inlet and outlet ports. The middle layer of the 50-μm-thick elastomeric membrane was purchased (BD Film KYQ50, Hangzhou Guinie Advanced Materials Company, China). After oxygen plasma treatment (PDC-002, Harrick Plasma, USA), these layers were assembled, bonded to a glass substrate, and then baked on a hot plate (C-MAG HP7, IKA, Germany) at 120°C for 10 min to enhance the bonding. During the plasma treatment, we used PDMS stamps to cover the check valve seat and corresponding area on the middle layer to ensure the normal function of check valve. The schematic illustration of the device fabrication process can be found in fig. S1.

Porous membrane filter

For the cell-removal circuit, track-etched PC membrane filters (pore size of 600 nm and membrane diameter of 25 mm; Whatman, Germany) were used. For the EV-isolation circuit, AAO isotropic membrane filters (pore size of 20 nm and membrane diameter of 13 mm; Whatman, Germany) were used. Scanning electron microscopy characterization of AAO membrane was shown in fig. S12.

Microfluidic circuit operation and flow rate measurement

Before filtration, the liquid layers of the cell-removal and EV-isolation circuits were filled with PBS to prevent the generation of bubbles during the process of pulsatile blood filtration. The whole blood sample (10-fold dilution) was loaded onto the PC membrane filter mounted on the cell-removal circuit, and the extracted plasma was injected into the AAO membrane filter integrated with the EV-isolation circuit. On the basis of the current microfluidic design, the volume of diluted blood sample inside the top microchamber was less than 150 μl. The cascaded microfluidic circuits were connected with pneumatic clock pulse generator to generate pulsatile flow at the membrane filter. The pneumatic clock pulse generator was constructed by an oil-free compressor (OTS-550, China) as a source of constant pneumatic pressure, a controller (OBKZN, Pneumatik doo, Japan) to adjust the magnitude of pressure, and a solenoid valve (8003, KUNAG, China) to periodically switch on and off the pneumatic pressure. Different clock frequencies, including 0.2, 0.5, and 1 Hz, were used with a fixed pneumatic pressure of 35 kPa (table S4). To quantify the time dependence of flow rates at the membrane filter (Q_{Filter}) and the filtrate outlet (Q_{Out}), a flow sensor (FS4, Fluidiclab, China) was connected to the top of membrane filter or the filtrate outlet for flow rate measurement with a time period up to 1000 s.

Dead-end filtration

To evaluate the filtration performance of dead-end filtration, the inlet of the membrane filter was connected with a constant pressure of 35 kPa, and the outlet was open to the atmosphere. For cell removal from whole blood samples, 600 μl of 10-fold–diluted whole blood was loaded into the 600-nm PC membrane filter, and the filtration was driven by the constant pressure until the loaded sample was processed. For EV isolation from CCM, 3 ml of the CCM was loaded into the 20-nm AAO membrane filter, and the filtration was driven by the constant pressure until the sample was concentrated to 200 μl.

CFD simulation

To evaluate the particulate flow during the filtration, the fluid field and particle motion induced by the fluid field were solved by the governing equations (incompressible Navier-Stokes equations of fluid flow and Newton's second law of particle motion)

$$\begin{aligned} \nabla \cdot \mathbf{u} &= 0 \\ \tfrac{\partial \mathbf{u}}{\partial t} + (\mathbf{u} \cdot \nabla \mathbf{u}) &= -\tfrac{1}{\rho}\nabla p + \nu \nabla^2 \mathbf{u} \\ m_{\mathrm{p}} \tfrac{dU_{\mathrm{p}}}{dt} &= \int_{\Sigma} (-p\mathbf{1} + \tau) \cdot \mathbf{n} d\sigma \\ \tfrac{d(\mathrm{I} \cdot \Omega_{\mathrm{p}})}{dt} &= \int_{\Sigma} (\mathbf{x} - \mathbf{x}_{\mathrm{cm}}) \times [(-p\mathbf{1} + \tau) \cdot \mathbf{n}] d\sigma \end{aligned} \quad (2)$$

where $\mathbf{u}$ is the fluid velocity, t is time, p is pressure, ρ is the fluid density, ν is the kinematic viscosity of the fluids, m_{p} is the particle mass, U_{p} is the velocity of particle, Ω_{p} is the particle rotate speed, $\mathbf{1}$ is the unit tensor, τ is the deviatoric stress tensor, $\mathbf{n}$ is normal vector of the particle surface, $\mathbf{I}$ is the moment of inertia tensor of the particle, $\mathbf{x}$ is the position of particle surface, and $\mathbf{x}_{\mathrm{cm}}$ is the position of the center of mass of the particle. The no-slip wall boundary conditions were imposed on the membrane and filter walls and particle surfaces. The membrane pore size was 20 nm, and the particles were represented by holes with a diameter of 100 nm. The averaged velocities were set to be 45 and 95 μm s^{-1} for the backflow and forward flow, respectively, which were corresponding to the case of a clock frequency of 0.5 Hz and a pneumatic pressure of 35 kPa. The equations were numerically solved on structured overlapping grids using Fluent 14.0 (ANSYS Inc., USA).

Calculation of removal efficiency of blood cells

To determine the removal efficiency of blood cells, an automatic cell counter (Countess 3, Invitrogen, USA) was used to quantify the cell content in the samples before and after the filtration by the cell-removal circuit. The samples diluted by 1000-fold (before filtration) and the extracted plasma without dilution (10 μl for each) were used for cell counting. The removal efficiency was determined as

$$\text{Removal efficiency} = 1 - \frac{C_{\mathrm{After}} V_{\mathrm{After}}}{1000 C_{\mathrm{Before}} V_{\mathrm{Before}}} \times 100\% \quad (3)$$

where C_{Before} and C_{After} were measured cell concentration in the samples before and after filtration, respectively, and V_{Before} and V_{After} were blood sample loading volume and extracted plasma volume, respectively.

Hemolysis analysis

The hemolysis levels of plasma samples obtained by the pulsatile filtration at various frequencies (0.2 to 1 Hz) and dead-end filtration were determined by measuring the absorption spectra of hemoglobin. Filtrated plasma samples (100 μl) were loaded to a 96-well plate, and the absorption spectra were obtained using a microplate reader (Synergy H1, BioTek, USA) in a range of 500 to 600 nm at 1-nm intervals. A 10-fold–diluted whole blood sample treated by 0.1% Triton X-100 and PBS was used as positive and negative controls, respectively.

Maximum volume of blood separation

To determine the maximum volume capable of blood separation by the device, 3.3 ml of diluted whole blood samples (10-fold dilution) was continuously processed for 120 min, while no notable membrane fouling was observed as determined by the plot of inverse flow rate against filtration volume (fig. S5).

Membrane replacement

After blood or EV separation, the 25- or 13-mm plastic filter holder (25 mm, 1214250, GSV Life Sciences, USA; 13 mm, SX0001300, Swinnex, China) was opened to remove the used PC or AAO membrane. The filter holder was then cleaned by washing and air drying, and a PC or AAO membrane was mounted into the filter holder for use (fig. S11A). To clean the microfluidic device, air was first injected into the microchannel to remove the residual, and PBS was injected for washing the device (fig. S11B).

Cell line

Human breast cancer cell lines (MCF-7 and SK-BR-3) and human mammary epithelial cell line (MCF-10A) were purchased from the American Type Culture Collection (USA). MCF-7 cells were cultured in minimum essential medium (C12571500BT, Gibco, USA), SK-BR-3 cells were cultured in McCoy's 5A medium (KGM4892-500, KeyGEN BioTECH, China), and MCF-10A cells were cultured in mammary epithelium basal medium (CC-3151, Lonza, Switzerland). All cells were cultured at 37°C with 5% CO_2.

EV isolation by UC

For isolation of cell line EVs, the cell culture media were collected until cells reached a confluency of 70%. The collected media were centrifuged first at 2000*g* for 10 min to remove cells and large debris. The resultant supernatant was centrifuged at 10,000*g* for 60 min, processed by a 0.22-μm membrane filtration (Millipore, USA), and ultracentrifuged at 100,000*g* for 90 min. The obtained EVs in each ultracentrifuge tube were recovered in 0.26 ml of PBS. Before UC, the weight between every pair of tubes was adjusted to be smaller than 0.05 g (*56*).

Transmission electron microscopy

MCF-7 EVs before and after pulsatile filtration were adsorbed on Formvar/carbon-coated copper grids for 30 min. The absorbed EVs were stained with five drops of 3% uranyl acetate. To obtain TEM images before filtration, the 10-fold–diluted whole blood was centrifuged at 2000*g* for 10 min to remove blood cells, adsorbed on Formvar/carbon-coated copper grids for 30 min, and stained with five drops of 3% uranyl acetate. The sample after filtration was adsorbed on Formvar/carbon-coated copper grids for 30 min and stained with five drops of 3% uranyl acetate. After drying by filter paper, the grids were observed on a TEM (G2 F20 S-TWIN, Tecnai, USA) at 200 kV.

Nanoparticle tracking analysis

To quantify the concentration and size distribution, samples containing EVs were characterized using NTA (NS300, Malvern Instrument, UK). The concentrations of particles were adjusted to 5×10^8 to 1×10^9 ml^{-1} for measurement to achieve optimal counting accuracy. The data of size distribution were captured and analyzed with the NTA 3.4 Analytical Software Suite.

Calculation of recovery rate

To determine the recovery rate of cell line EVs and blood plasma, the particle concentration before (C_{Before}) and after (C_{After}) various isolation methods (pulsatile filtration, dead-end filtration, and UC) were measured using NTA. To determine the recovery rate of blood EVs, the particle concentration before (C_{Before}) and after (C_{After}) the cascaded pulsatile filtration was measured using NTA. The whole blood samples were centrifuged at 2000*g* for 10 min to remove blood cells and used as the sample before filtration. The recovery rate was calculated as follows

$$\text{Recovery rate} = \frac{C_{After} V_{After}}{C_{Before} V_{Before}} \times 100\% \quad (4)$$

where V_{Before} and V_{After} were the sample loading volume and recovered volume, respectively.

Calculation of protein removal

To determine the removal efficiency of BSA using different PBS volumes for circulating washing, BSA concentrations in samples before (C_{PB}) and after (C_{PA}) pulsatile filtration using EV-isolation circuit were quantified using a commercial kit (bicinchoninic acid protein assay kit, Beyotime, China). To determine the removal efficiency of protein contents in whole blood samples, the protein concentrations in samples before (C_{PB}) and after (C_{PA}) the cascaded pulsatile filtration were quantified using the same kit. The whole blood samples were centrifuged at 2000*g* for 10 min to remove blood cells and used as the sample before filtration. The protein removal efficiency was calculated as follows

$$\text{Protein removal efficiency} = 1 - \frac{C_{PA} V_{After}}{C_{PB} V_{Before}} \times 100\% \quad (5)$$

where V_{Before} and V_{After} were the sample loading volume and recovered volume, respectively.

Calculation of removal efficiency of lipoproteins

To determine the removal efficiency of lipoproteins from whole blood, the contents of LDL and VLDL in samples before and after the cascaded pulsatile filtration were quantified by ELISA kits (HEB107Hu/SEB847Hu, Cloud-Clone, China). The whole blood samples were centrifuged at 2000*g* for 10 min to remove blood cells and used as the sample before filtration. For LDL quantification, the samples before and after filtration were diluted by 10^5- and 10^4-fold, respectively, for ELISA measurement. For VLDL quantification, the samples before and after filtration were diluted by 10^4- and 10^3-fold, respectively. The removal efficiency was determined as follows

$$\text{lipoprotein removal efficiency} = 1 - \frac{C_{LPA} V_{After} D_{After}}{C_{LPB} V_{Before} D_{Before}} \times 100\% \quad (6)$$

where C_{Before} and C_{After} were the concentrations of lipoproteins in samples before and after filtration, respectively, V_{Before} and V_{After} were the sample loading volume and recovered volume, respectively, and D_{Before} and D_{After} were the dilution folds of samples before and after filtration, respectively.

Western blot

Cell culture media (MCF-7, SK-BR-3, and MCF-10A) were concentrated to 200 μl and subjected to circulating washing (1 ml of PBS) using the EV-isolation circuit. Proteins (10 μg) extracted from lysed samples [by 1 × loading buffer at 100°C for 10 min, native–polyacrylamide gel electrophoresis (PAGE) loading buffer for CD63, and SDS-PAGE loading buffer for EpCAM, CD81, TSG101, and calnexin] and a standard ladder (PR1910, Solarbio, China) were separated on a gel (G2043, Servicebio, China) by electrophoresis (80 V for 30 min and 130 V for 60 min) in ice bath and transferred onto a polyvinylidene fluoride (PVDF) membrane. The PVDF membrane was blocked with a 5% BSA solution (A8010, Solarbio, China) in deionized water for 30 min at room temperature. After blocking, the membrane was incubated with anti-CD81 antibody (1000-fold diluted; ab109201, Abcam, UK), anti-TSG101 antibody (500-fold diluted; 102286-T38, Sino Biological, China), anti-calnexin antibody (1000-fold diluted; bsm-52639R, Bioss, China), anti-EpCAM antibody (1000-fold diluted; ab199521, Abcam, UK), and anti-CD63 antibody (1000-fold diluted; ab59479, Abcam, UK) at 4°C overnight and washed three times for 10 min using tris-buffered saline containing 0.5% Tween 20 (TBST) (table S5). The membrane was then incubated with a 5000-fold–diluted horseradish peroxidase (HRP)–conjugated anti-rabbit immunoglobulin G (IgG; ab6721, Abcam, UK) or a 5000-fold–diluted HRP-conjugated anti-mouse IgG (ab205719, Abcam, UK) at room temperature for 1 hour and washed three times for 10 min using TBST. Last, blots were visualized using chemiluminescence reagent (P0018FS, Beyotime, China). ImageJ (v1.53t, National Institutes of Health, USA) was used to quantify the protein band intensity. The raw images of WB films were converted into 8-bit grayscale format and subjected to "Subtract Background" and "Invert" operations in ImageJ. For each protein marker (row), a rectangular region of interest was selected to cover the largest band of the row. The protein band intensity was determined by subtracting the integrated gray value of background.

PEG-enhanced thermophoretic aptasensor

Isolated EVs (5 μl) were mixed with 2 mM $MgCl_2$, 7.5% PEG, and 100 nM aptamers targeting EpCAM or CD63 (Sangon Biotech, China) (table S6) in a final volume of 10 μl. The samples were immediately loaded in an 80-μm-thick microchamber (made by sandwiching an 80-μm-thick spacer between a bottom glass slide and a top sapphire slide) for pTAS detection without pretreatment. The microchamber was placed on an inverted fluorescent microscope (ECLIPSE Ti, Nikon, Japan), and the thermophoretic accumulation was achieved by focusing an infrared laser (1480 nm, 15 mW, Changchun Laser Optoelectronics Technology, China) on the glass slide for 10 min. The images before and after laser irradiation were captured by a 40× objective and an electron-multiplying charge-coupled device (Andor, UK).

Clinical cohort

The whole blood samples of patients with NMBC (n = 10) were collected from the Fifth Medical Center, Chinese People's Liberation Army (PLA) General Hospital and the Second Medical Center, Chinese PLA General Hospital. The whole blood samples of HD (n = 12) were collected from Beijing Sihui Traditional Chinese Medicine Hospital. All relevant ethical regulations were complied with. The study was approved by the Institutional Review Board of the Chinese PLA General Hospital. Informed written consent from all participants was obtained before the research (ages and molecular subtypes for patients with NMBC and HDs were summarized in table S7). A 10-fold–diluted whole blood (600 μl) was processed by the cascaded microfluidic circuits. The extracted plasma (200 μl) obtained by the cell-removal circuit was filtrated by the EV-isolation circuit with circulating washing (1 ml of PBS) and lastly concentrated to 100 μl (by performing an additional filtration step without circulating washing) for the pTAS assay.

Statistical analysis

The significance of differences in the expression levels from different groups of samples was tested using a two-tailed Mann-Whitney U test. To evaluate the performance in NMBC diagnosis, ROC analysis was carried out. Significance analyses, construction of ROC curve, and calculation of AUC were performed using GraphPad Prism 7 (GraphPad, USA).

Supplementary Materials

This PDF file includes:

Supplementary Notes
Figs. S1 to S12
Tables S1 to S7
Legend for movie S1
References

Other Supplementary Material for this manuscript includes the following:

Movie S1

View/request a protocol for this paper from *Bio-protocol*.

REFERENCES AND NOTES

1. G. van Niel, G. D'Angelo, G. Raposo, Shedding light on the cell biology of extracellular vesicles. *Nat. Rev. Mol. Cell Biol.* **19**, 213–228 (2018).
2. Q. Zhu, Y. Huang, Q. Yang, F. Liu, Recent technical advances to study metabolomics of extracellular vesicles. *Microchem. J.* **171**, 106816 (2021).
3. R. Kalluri, V. S. LeBleu, The biology, function, and biomedical applications of exosomes. *Science* **367**, eaau6977 (2020).
4. A. Möller, R. J. Lobb, The evolving translational potential of small extracellular vesicles in cancer. *Nat. Rev. Cancer* **20**, 697–709 (2020).
5. R. Xu, A. Rai, M. Chen, W. Suwakulsiri, D. W. Greening, R. J. Simpson, Extracellular vesicles in cancer — Implications for future improvements in cancer care. *Nat. Rev. Clin. Oncol.* **15**, 617–638 (2018).
6. B. Lin, Y. Lei, J. Wang, L. Zhu, Y. Wu, H. Zhang, L. Wu, P. Zhang, C. Yang, Microfluidic-based exosome analysis for liquid biopsy. *Small Methods* **5**, e2001131 (2021).
7. Y.-T. Kang, Z. Niu, T. Hadlock, E. Purcell, T.-W. Lo, M. Zeinali, S. Owen, V. G. Keshamouni, R. Reddy, N. Ramnath, S. Nagrath, On-chip biogenesis of circulating NK cell-derived exosomes in non-small cell lung cancer exhibits antitumoral activity. *Adv. Sci.* **8**, 2003747 (2021).
8. Y.-T. Kang, E. Purcell, C. Palacios-Rolston, T.-W. Lo, N. Ramnath, S. Jolly, S. Nagrath, Isolation and profiling of circulating tumor-associated exosomes using extracellular vesicular lipid–protein binding affinity based microfluidic device. *Small* **15**, e1903600 (2019).
9. K. S. Raju, Z. Niu, J. Marvar, S. Fortna, N.-E. Onukwugha, Y.-T. Kang, S. Nagrath, Abstract 2792: On-chip evaluation of cancer cell-extracellular vesicle interactions using a novel microfluidic microsystem (CellExoChip). *Cancer Res.* **82**, 2792 (2022).
10. F. Tian, C. Liu, J. Deng, J. Sun, Microfluidic separation, detection, and engineering of extracellular vesicles for cancer diagnostics and drug delivery. *Accounts Mater. Res.* **3**, 498–510 (2022).
11. H. Yan, Y. Li, S. Cheng, Y. Zeng, Advances in analytical technologies for extracellular vesicles. *Anal. Chem.* **93**, 4739–4774 (2021).

12. R. J. Lobb, M. Becker, S. Wen Wen, C. S. F. Wong, A. P. Wiegmans, A. Leimgruber, A. Möller, Optimized exosome isolation protocol for cell culture supernatant and human plasma. *J. Extracell. Vesicles* **4**, 27031 (2015).
13. H. Shao, H. Im, C. M. Castro, X. Breakefield, R. Weissleder, H. Lee, New technologies for analysis of extracellular vesicles. *Chem. Rev.* **118**, 1917–1950 (2018).
14. Y. Chen, Q. Zhu, L. Cheng, Y. Wang, M. Li, Q. Yang, L. Hu, D. Lou, J. Li, X. Dong, L. P. Lee, F. Liu, Exosome detection via the ultrafast-isolation system: EXODUS. *Nat. Methods* **18**, 212–218 (2021).
15. K. Brennan, K. Martin, S. P. FitzGerald, J. O'Sullivan, Y. Wu, A. Blanco, C. Richardson, M. M. Mc Gee, A comparison of methods for the isolation and separation of extracellular vesicles from protein and lipid particles in human serum. *Sci. Rep.* **10**, 1039 (2020).
16. K. R. Baillargeon, L. P. Murray, R. N. Deraney, C. R. Mace, High-yielding separation and collection of plasma from whole blood using passive filtration. *Anal. Chem.* **92**, 16245–16252 (2020).
17. Z. Wang, F. Li, J. Rufo, C. Chen, S. Yang, L. Li, J. Zhang, J. Cheng, Y. Kim, M. Wu, E. Abemayor, M. Tu, D. Chia, R. Spruce, N. Batis, H. Mehanna, D. T. W. Wong, T. J. Huang, Acoustofluidic salivary exosome isolation: A liquid biopsy compatible approach for human papillomavirus-associated oropharyngeal cancer detection. *J. Mol. Diagn.* **22**, 50–59 (2020).
18. D. Brambilla, L. Sola, A. M. Ferretti, E. Chiodi, N. Zarovni, D. Fortunato, M. Criscuoli, V. Dolo, I. Giusti, V. Murdica, K. Kluszczyńska, L. Czernek, M. Düchler, R. Vago, M. Chiari, E. V. Separation, EV separation: Release of intact extracellular vesicles immunocaptured on magnetic particles. *Anal. Chem.* **93**, 5476–5483 (2021).
19. S. Zhao, M. Wu, S. Yang, Y. Wu, Y. Gu, C. Chen, J. Ye, Z. Xie, Z. Tian, H. Bachman, P.-H. Huang, J. Xia, P. Zhang, H. Zhang, T. J. Huang, A disposable acoustofluidic chip for nano/microparticle separation using unidirectional acoustic transducers. *Lab Chip* **20**, 1298–1308 (2020).
20. A. Ozcelik, J. Rufo, F. Guo, Y. Gu, P. Li, J. Lata, T. J. Huang, Acoustic tweezers for the life sciences. *Nat. Methods* **15**, 1021–1028 (2018).
21. Y.-T. Kang, T. Hadlock, T.-W. Lo, E. Purcell, A. Mutukuri, S. Fouladdel, M. D. S. Raguera, H. Fairbairn, V. Murlidhar, A. Durham, S. A. McLean, S. Nagrath, Dual-isolation and profiling of circulating tumor cells and cancer exosomes from blood samples with melanoma using immunoaffinity-based microfluidic interfaces. *Adv. Sci.* **7**, 2001581 (2020).
22. S. Busatto, G. Vilanilam, T. Ticer, W.-L. Lin, D. W. Dickson, S. Shapiro, P. Bergese, J. Wolfram, Tangential flow filtration for highly efficient concentration of extracellular vesicles from large volumes of fluid. *Cell* **7**, 273 (2018).
23. P. Li, M. Kaslan, S. H. Lee, J. Yao, Z. Gao, Progress in exosome isolation techniques. *Theranostics* **7**, 789–804 (2017).
24. F. Liu, O. Vermesh, V. Mani, T. J. Ge, S. J. Madsen, A. Sabour, E.-C. Hsu, G. Gowrishankar, M. Kanada, J. V. Jokerst, R. G. Sierra, E. Chang, K. Lau, K. Sridhar, A. Bermudez, S. J. Pitteri, T. Stoyanova, R. Sinclair, V. S. Nair, S. S. Gambhir, U. Demirci, The exosome total isolation chip. *ACS Nano* **11**, 10712–10723 (2017).
25. H.-K. Woo, V. Sunkara, J. Park, T.-H. Kim, J.-R. Han, C.-J. Kim, H.-I. Choi, Y.-K. Kim, Y.-K. Cho, Exodisc for rapid, size-selective, and efficient isolation and analysis of nanoscale extracellular vesicles from biological samples. *ACS Nano* **11**, 1360–1370 (2017).
26. X. Luan, K. Sansanaphongpricha, I. Myers, H. Chen, H. Yuan, D. Sun, Engineering exosomes as refined biological nanoplatforms for drug delivery. *Acta Pharmacol. Sin.* **38**, 754–763 (2017).
27. I. L. Colao, R. Corteling, D. Bracewell, I. Wall, Manufacturing exosomes: A promising therapeutic platform. *Trends Mol. Med.* **24**, 242–256 (2018).
28. Z. A. Nizamudeen, R. Xerri, C. Parmenter, K. Suain, R. Markus, L. Chakrabarti, V. Sottile, Low-power sonication can alter extracellular vesicle size and properties. *Cell* **10**, 2413 (2021).
29. B. F. Hettich, J. J. Bader, J.-C. Leroux, Encapsulation of hydrophilic compounds in small extracellular vesicles: Loading capacity and impact on vesicle functions. *Adv. Healthc. Mater.* **11**, 2100047 (2022).
30. S.-J. Kim, R. Yokokawa, S. Cai Lesher-Perez, S. Takayama, Multiple independent autonomous hydraulic oscillators driven by a common gravity head. *Nat. Commun.* **6**, 7301 (2015).
31. Z. Li, S.-J. Kim, Autonomous microfluidic actuators for periodic sequential flow generation. *Sci. Adv.* **5**, eaat3080 (2019).
32. B. Mosadegh, C.-H. Kuo, Y.-C. Tung, Y.-S. Torisawa, T. Bersano-Begey, H. Tavana, S. Takayama, Integrated elastomeric components for autonomous regulation of sequential and oscillatory flow switching in microfluidic devices. *Nat. Phys.* **6**, 433–437 (2010).
33. Y. Lee, D.-M. Kim, Z. Li, D.-E. Kim, S.-J. Kim, Pulsatile plasma filtration and cell-free DNA amplification using a water-head-driven point-of-care testing chip. *Lab Chip* **18**, 915–922 (2018).
34. K. W. Oh, K. Lee, B. Ahn, E. P. Furlani, Design of pressure-driven microfluidic networks using electric circuit analogy. *Lab Chip* **12**, 515–545 (2012).
35. E. Roux, P. Bougaran, P. Dufourcq, T. Couffinhal, Fluid shear stress sensing by the endothelial layer. *Front. Physiol.* **11**, 861 (2020).
36. J. C. Schippers, J. Verdouw, The modified fouling index, a method of determining the fouling characteristics of water. *Desalination* **32**, 137–148 (1980).
37. A. Alhadidi, A. J. B. Kemperman, B. Blankert, J. C. Schippers, M. Wessling, W. G. J. van der Meer, Silt density index and modified fouling index relation, and effect of pressure, temperature and membrane resistance. *Desalination* **273**, 48–56 (2011).
38. S. F. E. Boerlage, M. D. Kennedy, M. R. Dickson, D. E. Y. El-Hodali, J. C. Schippers, The modified fouling index using ultrafiltration membranes (MFI-UF): Characterisation, filtration mechanisms and proposed reference membrane. *J. Membr. Sci.* **197**, 1–21 (2002).
39. T.-H. Kim, M. Lim, J. Park, J. M. Oh, H. Kim, H. Jeong, S. J. Lee, H. C. Park, S. Jung, B. C. Kim, K. Lee, M.-H. Kim, D. Y. Park, G. H. Kim, Y.-K. Cho, FAST: Size-selective, clog-free isolation of rare cancer cells from whole blood at a liquid–liquid interface. *Anal. Chem.* **89**, 1155–1162 (2017).
40. R. Linares, S. Tan, C. Gounou, N. Arraud, A. R. Brisson, High-speed centrifugation induces aggregation of extracellular vesicles. *J. Extracell. Vesicles* **4**, 29509 (2015).
41. J. Deng, F. Tian, C. Liu, Y. Liu, S. Zhao, T. Fu, J. Sun, W. Tan, Rapid one-step detection of viral particles using an aptamer-based thermophoretic assay. *J. Am. Chem. Soc.* **143**, 7261–7266 (2021).
42. J. Deng, S. Zhao, J. Li, Y. Cheng, C. Liu, Z. Liu, L. Li, F. Tian, B. Dai, J. Sun, One-step thermophoretic and gate operation on extracellular vesicles improves diagnosis of prostate cancer. *Angew. Chem. Int. Ed.* **61**, e202207037 (2022).
43. K. Lee, K. Fraser, B. Ghaddar, K. Yang, E. Kim, L. Balaj, E. A. Chiocca, X. O. Breakefield, H. Lee, R. Weissleder, Multiplexed profiling of single extracellular vesicles. *ACS Nano* **12**, 494–503 (2018).
44. G. Chen, A. C. Huang, W. Zhang, G. Zhang, M. Wu, W. Xu, Z. Yu, J. Yang, B. Wang, H. Sun, H. Xia, Q. Man, W. Zhong, L. F. Antelo, B. Wu, X. Xiong, X. Liu, L. Guan, T. Li, S. Liu, R. Yang, Y. Lu, L. Dong, S. McGettigan, R. Somasundaram, R. Radhakrishnan, G. Mills, Y. Lu, J. Kim, Y. H. Chen, H. Dong, Y. Zhao, G. C. Karakousis, T. C. Mitchell, L. M. Schuchter, M. Herlyn, E. J. Wherry, X. Xu, W. Guo, Exosomal PD-L1 contributes to immunosuppression and is associated with anti-PD-1 response. *Nature* **560**, 382–386 (2018).
45. Q. Zhu, L. Cheng, C. Deng, L. Huang, J. Li, Y. Wang, M. Li, Q. Yang, X. Dong, J. Su, L. P. Lee, F. Liu, The genetic source tracking of human urinary exosomes. *Proc. Natl. Acad. Sci. U.S.A.* **118**, e2108876118 (2021).
46. B. Lin, T. Tian, Y. Lu, D. Liu, M. Huang, L. Zhu, Z. Zhu, Y. Song, C. Yang, Tracing tumor-derived exosomal PD-L1 by dual-aptamer activated proximity-induced droplet digital PCR. *Angew. Chem. Int. Ed.* **60**, 7582–7586 (2021).
47. Y. Gu, C. Chen, Z. Mao, H. Bachman, R. Becker, J. Rufo, Z. Wang, P. Zhang, J. Mai, S. Yang, J. Zhang, S. Zhao, Y. Ouyang, D. T. W. Wong, Y. Sadovsky, T. J. Huang, Acoustofluidic centrifuge for nanoparticle enrichment and separation. *Sci. Adv.* **7**, eabc0467 (2021).
48. M. Wu, Y. Ouyang, Z. Wang, R. Zhang, P.-H. Huang, C. Chen, H. Li, P. Li, D. Quinn, M. Dao, S. Suresh, Y. Sadovsky, T. J. Huang, Isolation of exosomes from whole blood by integrating acoustics and microfluidics. *Proc. Natl. Acad. Sci. U.S.A.* **114**, 10584–10589 (2017).
49. S. Hassanpour Tamrin, A. Sanati Nezhad, A. Sen, Label-free isolation of exosomes using microfluidic technologies. *ACS Nano* **15**, 17047–17079 (2021).
50. W. Wang, J. Luo, S. Wang, Recent progress in isolation and detection of extracellular vesicles for cancer diagnostics. *Adv. Healthc. Mater.* **7**, e1800484 (2018).
51. M. Huang, L. Zhu, S. Kang, F. Chen, X. Wei, L. Lin, X. Chen, W. Wang, Z. Zhu, C. Yang, Y. Song, In situ visualization of PD-L1-specific glycosylation on tissue sections. *Anal. Chem.* **93**, 15958–15963 (2021).
52. J. Zhang, Y. Huang, M. Sun, S. Wan, C. Yang, Y. Song, Recent advances in aptamer-based liquid biopsy. *ACS Appl. Bio Mater.* **5**, 1954–1979 (2022).
53. Y. Pan, Z. Yang, C. Li, S. U. Hassan, H. C. Shum, Plant-inspired TransfOrigami microfluidics. *Sci. Adv.* **8**, eabo1719 (2022).
54. H. Yuan, J. Tian, Y. Chao, Y.-S. Chien, R.-H. Luo, J.-Y. Guo, S. Li, Y.-J. Chou, H. C. Shum, C.-F. Chen, Hand-powered microfluidics for parallel droplet digital loop-mediated isothermal amplification assays. *ACS Sens.* **6**, 2868–2874 (2021).
55. M. Yafia, O. Ymbern, A. O. Olanrewaju, A. Parandakh, A. Sohrabi Kashani, J. Renault, Z. Jin, G. Kim, A. Ng, D. Juncker, Microfluidic chain reaction of structurally programmed capillary flow events. *Nature* **605**, 464–469 (2022).
56. Z. Han, F. Wan, J. Deng, J. Zhao, Y. Li, Y. Yang, Q. Jiang, B. Ding, C. Liu, B. Dai, J. Sun, Ultrasensitive detection of mRNA in extracellular vesicles using DNA tetrahedron-based thermophoretic assay. *Nano Today* **38**, 101203 (2021).
57. R. J. Cornish, E. A. Milne, Flow in a pipe of rectangular cross-section. *Proc. R. Soc. London Ser. A-Math. Phys. Eng. Sci.* **120**, 691–700 (1928).
58. F. A. Perdigones, A. Luque, J. M. Quero, Correspondence between electronics and fluids in MEMS: Designing microfluidic systems using electronics. *IEEE Ind. Electron. Mag.* **8**, 6–17 (2014).
59. T. Baranyai, K. Herczeg, Z. Onódi, I. Voszka, K. Módos, N. Marton, G. Nagy, I. Mäger, M. J. Wood, S. El Andaloussi, Z. Pálinkás, V. Kumar, P. Nagy, Á. Kittel, E. I. Buzás, P. Ferdinandy, Z. Giricz, Isolation of exosomes from blood plasma: Qualitative and

quantitative comparison of ultracentrifugation and size exclusion chromatography methods. *PLOS ONE* **10**, e0145686 (2015).

60. V. Sunkara, C.-J. Kim, J. Park, H.-K. Woo, D. Kim, H. K. Ha, M.-H. Kim, Y. Son, J.-R. Kim, Y.-K. Cho, Fully automated, label-free isolation of extracellular vesicles from whole blood for cancer diagnosis and monitoring. *Theranostics* **9**, 1851–1863 (2019).
61. D. Buschmann, B. Kirchner, S. Hermann, M. Märte, C. Wurmser, F. Brandes, S. Kotschote, M. Bonin, O. K. Steinlein, M. W. Pfaffl, G. Schelling, M. Reithmair, Evaluation of serum extracellular vesicle isolation methods for profiling miRNAs by next-generation sequencing. *J. Extracell. Vesicles* **7**, 1481321 (2018).
62. R. E. Veerman, L. Teeuwen, P. Czarnewski, G. Güclüler Akpinar, A. Sandberg, X. Cao, M. Pernemalm, L. M. Orre, S. Gabrielsson, M. Eldh, Molecular evaluation of five different isolation methods for extracellular vesicles reveals different clinical applicability and subcellular origin. *J. Extracell. Vesicles* **10**, e12128 (2021).
63. R. Stranska, L. Gysbrechts, J. Wouters, P. Vermeersch, K. Bloch, D. Dierickx, G. Andrei, R. Snoeck, Comparison of membrane affinity-based method with size-exclusion chromatography for isolation of exosome-like vesicles from human plasma. *J. Transl. Med.* **16**, 1 (2018).

Acknowledgments

Funding: This work was supported by the National Natural Science Foundation of China (grant nos. 22025402, 22227805, T2222008, 22104026, and 22174030), the National Key R&D Program of China (grant nos. 2020YFA0210800 and 2021YFA0909400), the Strategic Priority Research Program of the Chinese Academy of Sciences (grant no. XDB36020300), and the CAS Project for Young Scientists in Basic Research (grant no. YSBR-036). **Author contributions:** Conceptualization: J.S. and Z.L. Methodology: Z.L. and J.S. Investigation: Z.L., Y.C., J.D., Y.L., L.B., L.Q., H.M., M.Z., F.T., and S.Z. Visualization: Z.L., C.L., and F.T. Supervision: J.S., S.Z., and F.T. Writing—original draft: J.S., Z.L., and C.L. Writing—review and editing: J.S. **Competing interests:** The authors declare that they have no competing interests. **Data and materials availability:** All data needed to evaluate the conclusions in the paper are present in the paper and/or the Supplementary Materials.

Submitted 5 August 2022
Accepted 16 March 2023
Published 21 April 2023
10.1126/sciadv.ade2819